

# “Near Ground” Vertical Vorticity in Supercell Thunderstorm Models

RICHARD ROTUNNO

*National Center for Atmospheric Research,<sup>a</sup> Boulder, Colorado*

PAUL M. MARKOWSKI

*Department of Meteorology, The Pennsylvania State University, University Park, Pennsylvania*

GEORGE H. BRYAN

*National Center for Atmospheric Research,<sup>a</sup> Boulder, Colorado*

(Manuscript received 11 October 2016, in final form 6 March 2017)

## ABSTRACT

Numerical models of supercell thunderstorms produce near-ground rotation about a vertical axis (i.e., vertical vorticity) after the development of rain-cooled outflows and downdrafts. The physical processes involved in the production of near-ground vertical vorticity in simulated supercells have been a subject of discussion in the literature for over 30 years. One cause for this lengthy discussion is the difficulty in applying the principles of inviscid vorticity dynamics in a continuous fluid to the viscous evolution of discrete Eulerian simulations. The present paper reports on a Lagrangian analysis of near-ground vorticity from an idealized-supercell simulation with enhanced vertical resolution near the lower surface. The parcel that enters the low-level maximum of vertical vorticity has a history of descent during which its horizontal vorticity is considerably enhanced. In its final approach to this region, the parcel's enhanced horizontal vorticity is tilted to produce vertical vorticity, which is then amplified through vertical stretching as the parcel rises. A simplified theoretical model is developed that exhibits these same features. The principal conclusion is that vertical vorticity at the parcel's nadir (its lowest point), although helpful, does not need to be positive for rapid near-surface amplification of vertical vorticity.

## 1. Introduction

The qualifier “near ground” for vertical vorticity is used in studies of supercell thunderstorms to distinguish processes that produce supercell rotation about a vertical axis at midtropospheric levels, or midlevels, from those near Earth's surface (Markowski and Richardson 2010, 224–233). Figure 1, adapted from Klemp (1987) and Markowski and Richardson (2010), illustrates how the midlevel supercell updraft is fed primarily by air parcels, such as parcel A, originating in an environment characterized by vertical wind shear or horizontally oriented vorticity. This horizontal vorticity on parcel A is redirected to the vertical as it encounters the supercell updraft and

accounts for its midlevel rotation. Figure 1 further illustrates how the flow in a supercell is arranged such that precipitation falls to the side of the updraft; evaporation of this precipitation cools the air near ground level and thus sets up a thermal boundary at the surface. This thermal boundary produces horizontal vorticity on air parcels, such as parcel B, that are flowing near the ground toward the updraft; this horizontal vorticity is also redirected upward beneath the main storm updraft and enhances the updraft rotation about a vertical axis near ground level. It has been argued that the redirection of horizontal vorticity to the vertical occurs on air parcels, such as parcel C, which are still descending as they approach the updraft and thus arrive near ground level with positive vertical vorticity as they enter the updraft. In this paper, we seek to clarify the near-surface vorticity dynamics<sup>1</sup> of simulated supercells

---

<sup>a</sup>The National Center for Atmospheric Research is sponsored by the National Science Foundation.

---

*Corresponding author e-mail:* Richard Rotunno, rotunno@ucar.edu

---

<sup>1</sup>In the absence of boundary layer effects, consistent with the models upon which Fig. 1 is based.

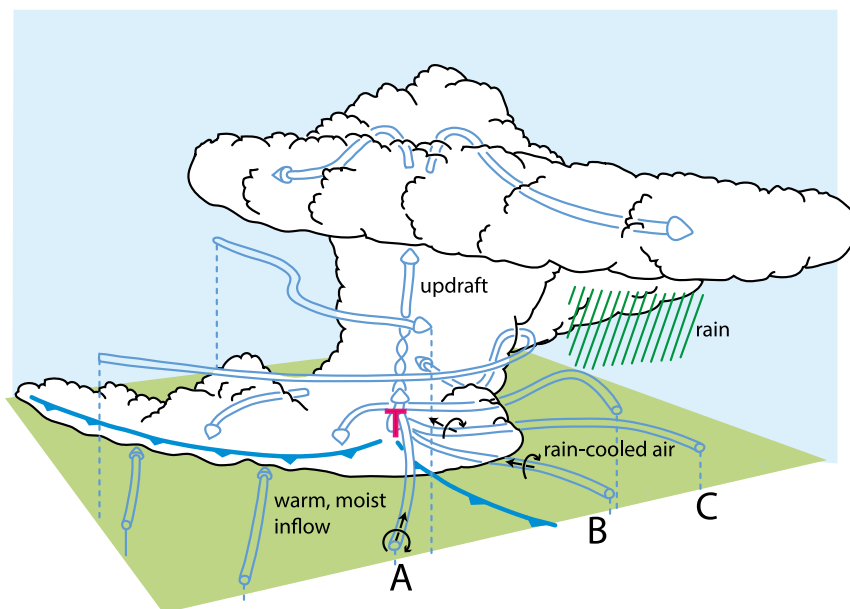


FIG. 1. Schematic diagram of the airflow and rotational features in a supercell thunderstorm. The letter T marks the typical location of tornado development within the supercell.

through an examination of the Lagrangian history of a parcel reaching the point of maximum near-ground vertical vorticity in an idealized numerical simulation and in a further-simplified theoretical model.

One clear difference between midlevel processes and near-ground-level processes in the supercell is the surface-based cold pool that baroclinically produces a horizontal component of vorticity along its edge (Klemp and Rotunno 1983; Rotunno and Klemp 1985). As described in Klemp (1987), this baroclinically produced horizontal vorticity is directed toward the supercell updraft, where it is tilted to the vertical and amplified by vortex stretching (parcel B, Fig. 1). Through analysis of numerical simulations like those of Rotunno and Klemp (1985), Davies-Jones and Brooks (1993) argue that, because of continued baroclinic production of horizontal vorticity, the streamlines and local vorticity vector become misaligned such that near-ground vertical vorticity is produced by upward tilting of horizontal vorticity on descending air parcels (parcel C, Fig. 1). The fluid parcel thus arrives at its lowest point with positive vertical vorticity that will be amplified through stretching as it enters the updraft. The relevance of this last point to near-ground vertical vorticity in simulated supercells is the subject of the present study.

Evaluation of these ideas, based on inviscid fluid dynamics described by Lagrangian material points, through analysis of diffusive, finite-difference numerical simulations is problematic. For example, Dahl et al. (2012) show the extreme sensitivity of trajectory analysis for air parcels

passing close to the low-level vertical vorticity maximum in simulated supercells (like point T in Fig. 1). Moreover, all numerical simulations of supercells enforce a condition on the viscous stress at the ground, which further complicates comparisons with the idealized concepts of near-ground vertical vorticity (Dahl et al. 2014, section 3). In view of the latter complications, recently published Lagrangian vorticity analyses of supercell simulations are typically restricted to the maximum vertical vorticity at the lowest interior grid point to which a parcel descends (Markowski et al. 2014; Markowski and Richardson 2014, hereafter MR14; Dahl et al. 2014; Dahl 2015). However, the absolute maximum vertical vorticity in the domain can be found in the updraft at the lowest model grid point, implying that air parcels travel there from below, and, cognizant of the problems discussed in Dahl et al. (2014), the absolute maximum vertical vorticity is not analyzed in these recent papers. Hence, we are motivated to ask how the near-ground absolute maximum vertical vorticity should behave under the conditions of the idealized Lagrangian fluid dynamics referenced in the preceding paragraph.

In the present work, we introduce a simple theoretical model in an attempt to clarify the behavior of the near-ground vertical vorticity as a parcel descends to its nadir and then rises up to its point of maximum vertical vorticity. We will refer to this last segment of the Lagrangian history of the parcel that is to acquire maximum near-ground vertical vorticity as the *final approach*.

In the next section, we examine the Lagrangian vorticity budget computed from a numerical simulation of

supercell-like flow following MR14, except with enhanced vertical resolution near the ground in an attempt to ameliorate some of the problems outlined above. In section 3, we develop a further-simplified theoretical model that we argue describes the main features of the near-ground vorticity evolution seen in the present idealized numerical simulations. The discussion and our conclusions are in section 4.

## 2. Lagrangian vorticity dynamics in an idealized-supercell simulation

In this section, we examine how vertical vorticity develops along near-surface trajectories within a supercell-like flow simulated in the toy model of MR14. In the MR14 model, an updraft and a downdraft are driven by a stationary heat source and sink, respectively; the updraft rotates cyclonically at midlevels owing to the vertically sheared environmental wind profile, in which winds turn clockwise with height. However, appreciable vertical vorticity does not develop at the lowest levels until cool outflow emanating from the heat sink underspreads the updraft. Of interest is MR14's Sc8m8 simulation (see their Figs. 5–13), which has strong environmental low-level shear and a moderately strong heat sink (i.e., the heat sink amplitude is  $S_{c0} = -0.008 \text{ K s}^{-1}$ , and the low-level shear parameter is  $m = 8$ , using the symbology of MR14). An intense, tornado-like vortex develops approximately 2600 s into the simulation.

The development of vorticity along a trajectory bound for the near-surface cyclonic vorticity maximum is analyzed in MR14's Fig. 11 (the lowest scalar level was at  $\hat{z} = 50 \text{ m}$ )<sup>2</sup>. The initial direction of the MR14 trajectory is from the southeast in the far-field storm environment (MR14's Fig. 11b); upon reaching the cool-air boundary, a combination of baroclinic generation and leftward turning of the trajectory brings the horizontal projections of the trajectory and the vorticity vector into alignment with each other and with the cool-air boundary. During the final 5 min, the trajectory descends, and the vertical component of the vorticity evolves toward its maximum value (MR14's Fig. 11a). As mentioned in section 1, we refer to this last part of the Lagrangian history as the final approach.

A closer look at the final approach of an air parcel toward the near-surface cyclonic vorticity maximum is obtained by rerunning the MR14 simulation with increased vertical resolution near the surface. Cloud Model 1 [CM1; see the appendix of Bryan and

Morrison (2012)], release 18, is used. As in MR14, the domain is  $100 \times 100 \times 10 \text{ km}^3$ , with rigid, free-slip,<sup>3</sup> top and bottom boundaries and open lateral boundaries. The horizontal grid spacing is 100 m within a  $20 \times 20 \text{ km}^2$  region centered in the domain and gradually increases to 3.9 km from the edge of this inner region to the lateral boundaries. Increased vertical resolution is employed near the surface, relative to MR14; the vertical grid spacing varies from 2 m in the lowest 50 m (the lowest scalar level is at  $\hat{z} = 1 \text{ m}$ ) to 380 m at the top of the domain. The large (small) time step is 0.10 (0.0125) s.

The rerun simulation is qualitatively similar to the original MR14 simulation. Figure 2 shows the perturbation potential temperature and horizontal vorticity fields at  $\hat{z} = 1$  and  $\hat{z} = 31 \text{ m}$  at 2500 s, along with the horizontal projection of a trajectory that approaches the developing tornado-like vortex (the trajectory is computed during the running of the model, and its position is updated every large time step). At  $\hat{z} = 1$  (31) m, the vertical vorticity  $\hat{\zeta}$  exceeds  $0.02$  ( $0.15$ )  $\text{s}^{-1}$ . The cyclonic vorticity maximum lies on the cool side of the boundary separating environmental air from the cool outflow emanating from the heat sink, and the cool air is beginning to “wrap up” in much the same way as a hook echo in a tornadic supercell observed by radar (Figs. 2a,b). The horizontal vorticity is considerably larger on the cool side of the outflow boundary than in the environment (Figs. 2c,d), especially in the lowest few meters, where the horizontal vorticity magnitude exceeds  $1 \text{ s}^{-1}$  within a channel on the immediate cool side of the outflow boundary. The horizontal vorticity is highly streamwise within the airstreams feeding the near-surface cyclonic vorticity maximum (e.g., note the alignment of the vectors overlaid in Figs. 2a and 2c).

The trajectory highlighted in Fig. 2 follows a path similar to the trajectory in MR14's Fig. 11, though we only focus on a 3-min period (2336–2516 s) that includes the parcel's final approach and early passage through the cyclonic vorticity maximum that eventually becomes a tornado-like vortex. At the start of this time period, the parcel's  $\hat{\zeta}$  is small and negative but is slowly increasing as the parcel gradually descends (Figs. 3a–c). The positive  $\hat{\zeta}$  trend is attributable to positive stretching ( $\hat{\zeta}$  and  $\partial\hat{w}/\partial\hat{z}$  are both negative).

<sup>2</sup> Here and throughout a hatted variable refers to a dimensional quantity.

<sup>3</sup> “Free slip” here means that the vertical derivative of the horizontal stress components is set to zero at the lower surface (Klemp and Wilhelmson 1978). We note that CM1 versions 16 and earlier had the horizontal stress set to zero at the surface as the default option.

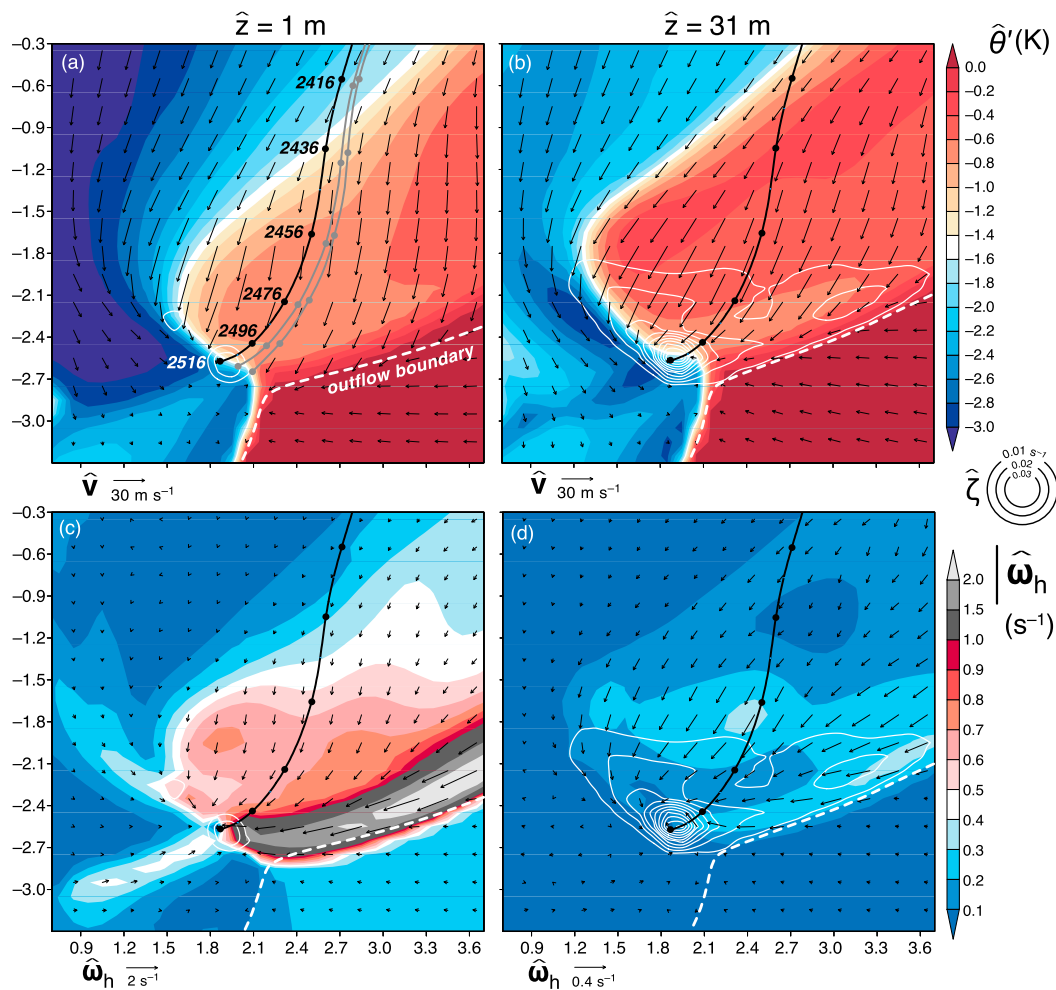


FIG. 2. (a),(b) Horizontal cross sections of potential temperature perturbation  $\hat{\theta}'$  (shaded), vertical vorticity  $\hat{\zeta}$  (contoured every  $0.01 \text{ s}^{-1}$  starting at  $0.01 \text{ s}^{-1}$ ), and horizontal storm-relative winds (black vectors located at every other grid point) at  $\hat{t} = 2500 \text{ s}$  at (a)  $\hat{z} = 1$  and (b)  $\hat{z} = 31 \text{ m}$  in the rerun of MR14's Sc8m8 pseudostorm simulation. The trajectory analyzed in Fig. 3 is indicated with the heavy black line, with markers placed at 20-s intervals. (c),(d) As in (a) and (b), respectively, but the horizontal vorticity magnitude  $|\hat{\omega}_h|$  (shaded) and horizontal vorticity vectors  $\hat{\omega}_h$  are shown [note that their scaling differs in (c) and (d)]. The two gray trajectories shown in (a), which sample different parts of the vertical vorticity, have Lagrangian vorticity budgets very similar to that shown in the following figure.

When the parcel reaches its nadir at  $\hat{z} = 2.3 \text{ m}$ , its  $\hat{\zeta} \approx 0$  (Fig. 3c), though  $D\hat{\zeta}/D\hat{t}$  remains positive. Vorticity stretching vanishes here ( $\partial\hat{w}/\partial\hat{z} = 0$ ), but tilting is large and positive (Fig. 3e), owing to the large horizontal vorticity of the parcel ( $>0.5 \text{ s}^{-1}$ ), which is an order of magnitude larger than in the environment (Figs. 2c, 3d). The positive tilting at the trajectory's nadir is crucial for the acquisition of positive  $\hat{\zeta}$  because stretching alone cannot cause  $\hat{\zeta}$  to go from negative to positive values. Thereafter, once positive  $\hat{\zeta}$  is obtained, stretching once again goes positive ( $\hat{\zeta}$  and  $\partial\hat{w}/\partial\hat{z}$  are both positive), and  $\hat{\zeta}$  eventually grows explosively (Fig. 3e). The parcel attains a  $\hat{\zeta}$  of  $0.001$ ,  $0.01$ , and  $0.10 \text{ s}^{-1}$  by the time it has

ascended to altitudes of  $\hat{z} = 3.0$ ,  $7.2$ , and  $16.1 \text{ m}$ , respectively (Figs. 3a,b).

### 3. A simplified Lagrangian model

#### a. Parcel trajectories

To develop a quantitative analytical model of the vorticity following a fluid parcel in the final approach, we consider a simplified model of the final-approach flow ( $\hat{u}$ ,  $\hat{w}$ ) in an  $\hat{x}$ - $\hat{z}$  plane aligned with the cool-air boundary (i.e., along a trajectory like B or C) of Fig. 1. By definition, the variation of buoyancy is zero along

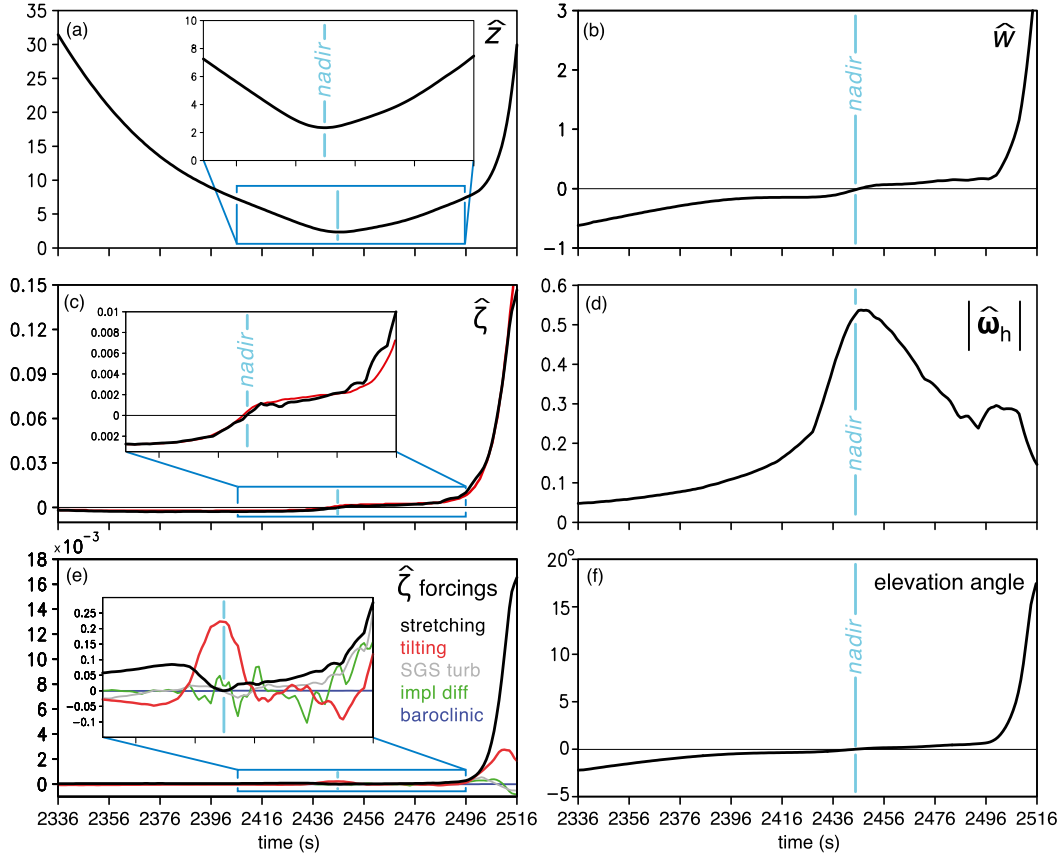


FIG. 3. The (a) altitude  $\hat{z}$  (m), (b) vertical velocity  $\hat{w}$  ( $\text{m s}^{-1}$ ), (c) vertical vorticity  $\hat{\zeta}$  ( $\text{s}^{-1}$ ), (d) horizontal vorticity magnitude  $|\hat{\omega}_h|$  ( $\text{s}^{-1}$ ), (e) vertical vorticity forcings ( $\times 10^{-3} \text{ s}^{-2}$ ), and (f) elevation angle ( $^\circ$ ) of the velocity vector with respect to horizontal along the trajectory identified in Fig. 2. In (c), the black curves are  $\hat{\zeta}$  interpolated to the parcel, and the red curves are  $\hat{\zeta}$  obtained by integrating the  $\hat{\zeta}$  forcings shown in (e).

the cool-air boundary; if we further assume the flow is steady, inviscid, incompressible, and independent of  $\hat{y}$ , then the governing equation for this flow is

$$J(\hat{\eta}, \hat{\psi}) = 0, \tag{1}$$

where  $J(\hat{a}, \hat{b})(\equiv \partial_{\hat{x}}\hat{a}\partial_{\hat{z}}\hat{b} - \partial_{\hat{z}}\hat{a}\partial_{\hat{x}}\hat{b})$  is the Jacobian and the  $\hat{y}$ -directed vorticity  $\hat{\eta} = \partial_{\hat{z}}\hat{u} - \partial_{\hat{x}}\hat{w} = (\partial_{\hat{z}\hat{z}} + \partial_{\hat{x}\hat{x}})\hat{\psi}$ , since the velocity field  $(\hat{u}, \hat{w}) = (\partial_{\hat{z}}\hat{\psi}, -\partial_{\hat{x}}\hat{\psi})$  by virtue of incompressibility. The major approximation in this analysis is that the final-approach flow is independent of the  $\hat{y}$  direction. Although the flow is not independent of  $\hat{y}$  (Figs. 2a,b), the present model results will be shown to agree rather well with the Lagrangian vorticity analysis from the idealized simulations presented in section 2.

It may be verified that

$$\hat{\psi}(\hat{x}, \hat{z}) = -\psi_0 \cos k\hat{x} \sin m\hat{z} \tag{2}$$

is a solution to (1). The parameters  $\psi_0$ ,  $k \equiv 2\pi/\lambda_x$  and  $m \equiv 2\pi/\lambda_z$  specify, respectively, the amplitude and the

horizontal and vertical scales of motion. For  $\psi_0 > 0$ , (2) describes sinking motion for  $\hat{x} > 0$  and rising motion for  $\hat{x} < 0$ . Based on the simulations of the previous section, we estimate  $\lambda_x \approx 5000 \text{ m}$  and  $\lambda_z \approx 2000 \text{ m}$  so that (2) describes a motion that reaches its maximum/minimum vertical velocity at  $\hat{z} = 500 \text{ m}$  ( $=\lambda_z/4$ ). With the latter parameters, we consider (2) as a crude model for the final-approach flow that would exist below cloud base in an actual supercell.

The equation for the velocity in the  $\hat{y}$  direction,  $\hat{v}(\hat{x}, \hat{z}, \hat{t})$ , under the assumptions the flow is inviscid, incompressible, and independent of  $\hat{y}$ , is

$$\frac{\partial \hat{v}}{\partial \hat{t}} + J(\hat{v}, \hat{\psi}) = 0. \tag{3}$$

In principle, the baroclinic production of vorticity should be included here since the buoyancy varies in the  $\hat{y}$  direction; however, analyses such as that of Fig. 11 of MR2014 and Dahl et al. (2014, p. 3037) show that this term is negligible in the final approach. The time

dependence of  $\hat{v}$  is retained, as it provides a simple way to compare and contrast solutions with different initial distributions of the vorticity  $(\hat{\xi}, \hat{\zeta}) = (-\partial_{\hat{z}}\hat{v}, \partial_{\hat{x}}\hat{v})$  in the  $\hat{x}$ - $\hat{z}$  plane. Note that in the present model  $\hat{\psi}$  determines the evolution of  $\hat{v}$  but there is no feedback from  $\hat{v}$  to  $\hat{\psi}$ .

Although one can obtain analytical solutions based on (2) for the projection in the  $\hat{x}$ - $\hat{z}$  plane of fluid-parcel trajectories, these solutions are complicated. Hence, to illuminate the basic processes, we consider (2) in the vicinity of the nadir close to the ground (i.e., in the limit  $k\hat{x} \ll 1, m\hat{z} \ll 1$ ), where, by virtue of a Taylor series expansion of the trigonometric functions in (2),  $\hat{\psi}$  takes the form

$$\hat{\psi}(\hat{x}, \hat{z}) = -\psi_0 \left[ 1 - \frac{(k\hat{x})^2}{2} \right] \left[ m\hat{z} - \frac{(m\hat{z})^3}{3!} \right]. \quad (4)$$

With the dimensional parameters  $\psi_0, k$ , and  $m$  defined, it will be convenient to use them to nondimensionalize the equations. With some hindsight, we let

$$(u, w) \equiv \left( \frac{\hat{u}}{u_0}, \frac{\hat{w}}{u_0} \right), \quad x \equiv \frac{k\hat{x}}{\sqrt{2}}, \quad z \equiv \frac{k\hat{z}}{\sqrt{2}}, \quad \text{and} \quad t \equiv \frac{ku_0\hat{t}}{\sqrt{2}}, \quad (5)$$

where  $u_0 \equiv \psi_0 m$ . Using these, the nondimensional velocity field is

$$(u, w) = (-1 + x^2, -2xz) + O(z^2). \quad (6)$$

The phrase ‘‘near-ground vorticity’’ is used throughout the literature on this topic. The definition is vague as it can only be roughly defined by the processes that occur near the ground. Since we are dealing with the discussion of supercell rotation excluding boundary layer processes, the cold pool is the only physical near-ground process. However, as mentioned above, in the final approach baroclinic processes are no longer contributing to the vorticity and the dynamics are essentially barotropic. Hence, the only remaining near-ground effect is the presence of the solid lower boundary at which  $w = 0$ . Therefore, we think the only definition that more or less encompasses the collective understanding is as follows: near-ground means near enough to the ground for  $w \propto z$  to hold. In keeping with this definition, we consider flows for which  $z^2 \ll 1$  and neglect the last term in (6).

For each point  $(x, z)$  in (6), one can define the parcel that occupied positions  $(x_i, z_i)$  at the earlier time  $t = t_i$ : that is,

$$[x(t), z(t)] = [x(x_i, z_i, t), z(x_i, z_i, t)]. \quad (7)$$

The Lagrangian velocity of each point is  $(dx/dt, dz/dt)$ , where the derivative is taken holding  $(x_i, z_i)$  constant

(Dutton 1976, chapter 5.7). Equating this Lagrangian velocity to the Eulerian velocity in (6) gives

$$\left( \frac{dx}{dt}, \frac{dz}{dt} \right) = (-1 + x^2, -2xz). \quad (8)$$

The first member of (8) is independent of  $z$  and can be integrated directly to give

$$x(t) = \frac{1 + x_i - (1 - x_i)e^{2(t-t_i)}}{1 + x_i + (1 - x_i)e^{2(t-t_i)}}. \quad (9)$$

With (9), the solution to the second member of (8) is

$$z(t) = \frac{z_i}{4} e^{-2(t-t_i)} [1 + x_i + (1 - x_i)e^{2(t-t_i)}]^2. \quad (10)$$

Equations (9) and (10) represent a family of descending, and subsequently ascending, trajectories defined by  $(x_i, z_i, t_i)$ . If we fix the nadir at  $x(0) = 0$ , then (9) gives

$$x_i = \frac{1 - e^{2t_i}}{1 + e^{2t_i}}. \quad (11)$$

With (11), (10) can be written as

$$z(t) = z_i e^{-2(t-t_i)} \left( \frac{1 + e^{2t}}{1 + e^{2t_i}} \right)^2. \quad (12)$$

Figure 4a shows a sample trajectory in the  $x$ - $z$  plane; with the  $z$  coordinate normalized by  $z_i$ , (11) and (12) indicate the only input parameter is  $t_i$ . To estimate a value of  $t_i$  relevant to the analysis in Figs. 2 and 3, we need to estimate the dimensional time scale, which, from (5), is  $\tau \equiv \hat{t}t \equiv \sqrt{2}/(ku_0) \simeq 0.22\lambda_x/u_0$ ; as mentioned above, a rough estimate<sup>4</sup> gives  $\lambda_x \simeq 5000$  m. Figures 2 and 3 suggest  $u_0 \simeq 20$  m s<sup>-1</sup> at the nadir and therefore  $\tau \simeq 55$  s. Figure 3a indicates that the parcel takes approximately 50 s to descend from  $\hat{z} \simeq 8$  m (at  $\hat{t} = 2396$  s) to the nadir at  $\hat{z} \simeq 2.3$  m (at  $\hat{t} = 2446$  s); hence, we let  $t_i = -50$  s/55 s  $\simeq -0.9$ , and, by (11),  $x_i \simeq 0.72$  for the trajectory shown in Fig. 4a. From (12),  $z(0)/z_i \simeq 0.5$ , which is comparable to the analogous ratio for the analyzed trajectory in Fig. 3a (2.3 m/8 m  $\simeq 0.3$ ).

### b. Vorticity analysis

Under the foregoing assumptions, the nondimensional Lagrangian vorticity  $(\xi, \eta, \zeta)$  can be obtained from the

<sup>4</sup> An obvious shortcoming of the present model is the symmetric downdraft to updraft experienced by a parcel rather than the more realistic parcel flow from broad, weak downdrafts to narrow strong updrafts, as seen in Fig. 3b. Hence, there can only be a rough estimate of  $\lambda_x$ .

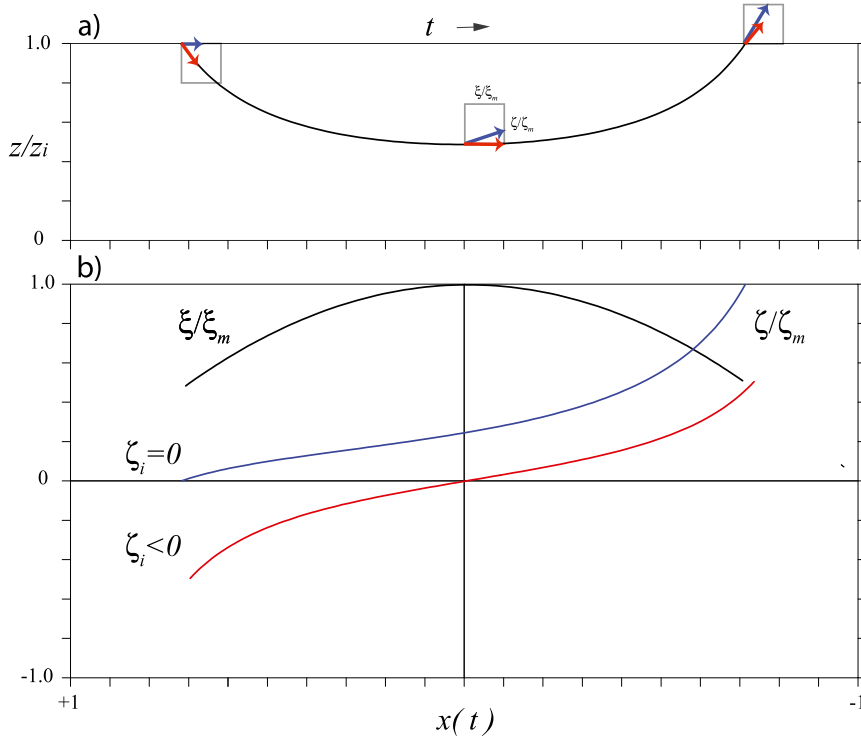


FIG. 4. (a) An air-parcel trajectory in the  $x$ - $z$  plane and (b)  $\xi(t)/\xi_m$ , the along-flow horizontal vorticity normalized by its maximum value (black curve), and  $\zeta(t)/\zeta_m$ , the vertical vorticity normalized by the maximum produced through the tilting/stretching term in (17) for  $\zeta_i = 0$  (blue curve) and  $\zeta_i < 0$  such that  $\zeta(0) = 0$  (red curve). The projection of the vorticity vector in the  $x$ - $z$  plane is plotted at three locations along the trajectory for the two cases in (a) [ $\zeta_i = 0$  (blue arrow);  $\zeta_i < 0$  (red arrow)]. Note that  $t$  increases and  $x(t)$  goes from positive to negative from left to right in both panels.

Cauchy formula (Dutton 1976, p. 385), which in the present notation is

$$\xi(t) = \frac{\partial x}{\partial x_i} \xi_i + \frac{\partial x}{\partial z_i} \zeta_i, \tag{13a}$$

$$\zeta(t) = \frac{\partial z}{\partial x_i} \xi_i + \frac{\partial z}{\partial z_i} \zeta_i, \quad \text{and} \tag{13b}$$

$$\eta(t) = \eta_i, \tag{13c}$$

where the terms involving  $\partial x/\partial y_i = \partial z/\partial y_i = 0$  are not written, and (13c) is a consequence of  $\partial y/\partial y_i = 1$ ; note also that (13c) is consistent with (1). With (9) and (10), the partial derivatives in (13a) and (13b) can be directly calculated.

Equation (13a) is particularly simple, as  $x(t)$  is independent of  $z_i$ , and therefore the only physical effect is vortex-line stretching in the  $x$  direction. Substituting (9) into (13a) yields

$$\xi(t) = \frac{4e^{2(t-t_i)}}{[1 + x_i + (1 - x_i)e^{2(t-t_i)}]^2} \xi_i, \tag{14}$$

which, in light of (10), implies

$$\frac{\xi(t)}{\xi_i} = \frac{z_i}{z(t)}. \tag{15}$$

The latter equation is a consequence of the continuity equation, which requires  $(\partial x/\partial x_i)(\partial z/\partial z_i) = 1$  for the flow under consideration. Based on this model, one expects the horizontal vorticity to be inversely proportional to the height of the fluid parcel, which is approximately true for the trajectory examined in Figs. 3a and 3d. Equation (15) underlines the importance of the descent phase of the final approach in producing large horizontal streamwise vorticity, consistent with the analysis of Adlerman et al. (1999).

Equation (13b) for the vertical component of vorticity reflects the integrated effect of vortex-line tilting and stretching following the parcel. The second term on the rhs of (13b) can be calculated from (10) simply as  $[z(t)/z_i]\zeta_i$ . Substituting (9) into (13b) and then using (11) to eliminate  $x_i$  in favor of  $t_i$  gives

$$\zeta(t) = z_i e^{-2(t-t_i)} \left( \frac{1 + e^{2t}}{1 + e^{2t_i}} \right) [1 - e^{2(t-t_i)}] \xi_i + \frac{z(t)}{z_i} \zeta_i. \tag{16}$$

A more suggestive form can be obtained by manipulation via (12) of the first term on the rhs to obtain

$$\zeta(t) = \frac{z(t)}{z_i} \left\{ -z_i \xi_i \left( \frac{1 + e^{2t_i}}{1 + e^{2t}} \right) [e^{2(t-t_i)} - 1] + \zeta_i \right\}. \quad (17)$$

Equation (17) would result from a straightforward solution of the Lagrangian equation for the vertical component of vorticity, which, in dimensionless form, and substituting for  $w$  from (6), is

$$\frac{d\zeta}{dt} = -2z\xi - 2x\zeta, \quad (18)$$

where the terms on the rhs are commonly referred to as the tilting and the stretching terms, respectively. In the present case, the tilting term  $-2z(t)\xi(t) = -2z_i\xi_i$  by virtue of (15) and is positive since  $\xi_i < 0$  (because the upstream baroclinic production term is proportional to  $\partial_y\hat{\theta} < 0$ , as suggested in Fig. 1) in our model of the final-approach flow. Thus, the solution to (18) can be expressed as

$$\zeta(t) = \exp \left[ - \int_{t_i}^t 2x(\tilde{t}) d\tilde{t} \right] \left\{ -2z_i\xi_i \int_{t_i}^t \exp \left[ \int_{t_i}^{\tilde{t}} 2x(\tilde{t}) d\tilde{t} \right] d\tilde{t} + \zeta_i \right\}; \quad (19)$$

[cf. (9) of Rotunno 1981] it is easy to show that the time-dependent terms inside and outside the curly braces are equal to their counterparts in (17).

### c. Examples

Figure 4b graphs the solutions for  $\xi(t)$  and  $\zeta(t)$  along the trajectory shown in Fig. 4a. The solution for  $\xi(t)$  is computed directly from (15) but normalized by its minimum value  $\xi_m \equiv [z_i/z(0)]\xi_i \simeq 2\xi_i$ . The solution for  $\zeta(t)$  is normalized by  $\zeta_m$ , the maximum value of the first term on the rhs of (16) (which occurs at  $t = -t_i$ ), since we will be interested in comparing solutions with different  $\zeta_i$ . Noting that  $z(-t_i)/z_i = 1$  and using (17), we define  $\zeta_m \equiv \zeta(-t_i) - \zeta_i = -z_i\xi_i[(1 + e^{2t_i})/(1 + e^{-2t_i})](e^{-4t_i} - 1)$ ; with  $t_i = -0.9$ ,  $\zeta_m \simeq -5.9z_i\xi_i$ . In the two examples shown in Fig. 4b, the nondimensional parameter  $-z_i\xi_i = -\hat{z}_i\xi_i/u_0 = -(8\text{ m})(-0.1\text{ s}^{-1})/20\text{ m s}^{-1} = 0.04$  ( $\xi_i$  at  $\hat{t} = 2396\text{ s}$  is estimated from Fig. 3d), and thus  $\zeta_m \simeq 0.24$ . In dimensional terms,  $\zeta_m = \zeta_m/(55\text{ s}) \simeq 0.004\text{ s}^{-1}$ , which is comparable to the values seen in Fig. 3c at  $\hat{t} = 2496\text{ s}$ .

With (16) in hand, we now address several issues that have been raised in the literature concerning near-ground vertical vorticity. The first term in the curly braces of (17) represents the production of vertical vorticity through the tilting of horizontal vorticity and

the vertical stretching of the vertical vorticity so produced; this term is positive with  $-z_i\xi_i > 0$  for the descending ( $t < 0$ ) portion of the parcel trajectory, as emphasized in Davies-Jones and Brooks (1993). If, owing to upstream baroclinic production, the vorticity vector has an upward inclination with respect to the trajectory at  $t_i$ , then (17) describes the subsequent evolution of  $[\xi(t), \zeta(t)]$  as a vector that descends to the surface “feet first” (Davies-Jones and Brooks 1993, p. 111). This feet-first landing is thought to be important, because it provides at the nadir  $\zeta > 0$ , which can be amplified through stretching as the parcel rises up from the nadir.

Motivated by the foregoing, we show in Fig. 4b the evolution of  $\zeta(t)$  with  $\zeta_i = 0$  and another evolution with  $\zeta_i < 0$  set so that there is zero vertical vorticity at the nadir [i.e. from (16),  $\zeta_i = 0.5z_i\xi_i(e^{-2t_i} - e^{2t_i})$ ]. The case with  $\zeta_i = 0$  (blue curve in Fig. 3b) is almost identical to Fig. 12 of Dahl et al. (2014). In this case, the initial vorticity vector is horizontal; tilting in downdraft produces an upward-pointing vorticity vector at the nadir, which then proceeds to amplify in updraft. The second case shown in Fig. 4b (red curve in Fig. 3b) has  $\zeta_i < 0$ ,  $\zeta(0) = 0$ , and  $\zeta(t)$  amplifying in updraft for  $t > 0$ . Although the maximum  $\zeta$  is reduced compared to the case with  $\zeta_i = 0$ , it is clear that the growth of vertical vorticity in updraft occurs whether or not there is positive vertical vorticity at the nadir. Inspection of (17) shows that the first term on the rhs is the growth engine and that it is independent of  $\zeta_i$ . That is, the second term can shift the vertical vorticity curves in Fig. 4b up or down, even producing  $\zeta(0) < 0$ , but  $\zeta(t)$  will still grow to positive values by virtue of the first term on the rhs of (17).

That the first term on the rhs of (17) is proportional to  $z_i\xi_i$  suggests that the most important physical process in the downdraft is the amplification of the streamwise vorticity. Perhaps more to the point is that sufficiently large  $\xi(0)$  can be tilted and stretched in updraft to produce large near-ground vorticity without the help of nonzero  $\zeta$  at the nadir. To see this, we let  $t_i = 0$  and  $\zeta_i = 0$  in (17) to obtain

$$\frac{\zeta(t)}{\xi_i} = 2z(t)x(t), \quad (20)$$

which, according to (8), is simply the slope of the trajectory near the nadir [note that  $\xi_i = \xi(0)$  in this example]. To put (20) into dimensional form, recall that  $\zeta = \tau\hat{\zeta}$  and  $\xi = \tau\hat{\xi}$ ; substituting for  $(x, z)$  from (5) gives

$$\hat{\zeta}(\hat{t}) = k^2 \hat{z}(\hat{t}) \hat{x}(\hat{t}) \hat{\xi}. \quad (21)$$

The wavenumber is estimated as in section 3a to give  $k^2 = (2\pi/5000\text{ m})^2 \simeq 1.6 \times 10^{-6}\text{ m}^{-2}$ . Judging from the

inset in Fig. 3a, from  $\hat{t} = 2446$  to 2496 s, the parcel rises approximately 5.3 m over a distance of roughly 900 m (according to Fig. 2a); Fig. 3d indicates  $\hat{\xi}_i \simeq 0.54 \text{ s}^{-1}$ , and therefore (21) predicts the vertical vorticity of the parcel to reach  $\hat{\zeta}(\hat{t} = 2496 \text{ s}) \simeq 0.004 \text{ s}^{-1}$ , which is comparable to the values shown in the inset of Fig. 3c.

#### 4. Discussion and conclusions

This work was motivated by the idea that  $\zeta > 0$  at the nadir is important to explain near-ground vertical vorticity in supercell thunderstorm models (Davies-Jones and Brooks 1993; Davies-Jones 2015). The two calculations shown by the red and blue curves in Fig. 4b can be thought of as respective prototypes for parcels B and C of Fig. 1. In both cases, there is a contribution to the increase of vertical vorticity through upward tilting of horizontal vorticity in the downdraft phase ( $t < 0$ ). However, the existence of trajectories such as those in the present simulations (Figs. 2, 3) and the corresponding analytical solution in Fig. 4b (red curve) show that rapid, near-surface amplification of  $\zeta(t)$  does not require  $\zeta > 0$  at the nadir of the trajectory. The present paper builds on the previous studies by using the idealized-supercell numerical model of MR14<sup>5</sup> and a simple Lagrangian model to reinforce the point that  $\zeta > 0$  at the nadir is not essential for near-ground vertical vorticity in simulated supercell thunderstorms.

The key process is the amplification of the horizontal streamwise vorticity during the descent phase of the final approach, which allows for large near-ground vertical vorticity through subsequent tilting and stretching in rising air. This process was identified in the budget analysis of Adlerman et al. (1999). An analytical example of this process can be found in the steady-state solutions for Beltrami flow developed in Davies-Jones (2008). The present case with  $\zeta = 0$  at the nadir shown in Fig. 4b is, in fact, a two-dimensional version of the latter [inspection of (3) indicates steady flow with  $\zeta = 0$  at the nadir]. The case with  $\zeta > 0$  at the nadir implies an evolving Eulerian field  $v(x, z, t)$ , which may be relevant to the developmental stage of near-ground supercell rotation but not to the steady-state flow depicted, for example, in Fig. 1.

There are a number of situations where a parcel descends near to the ground and then flows along without subsequent rising motion. For example, in their study of the formation of vortex sheets (i.e., shear lines) along

<sup>5</sup> Although MR14 (p. 257) attributes the rapid increase of near-ground  $\zeta$  to the stretching of  $\zeta$  facilitated by having  $\zeta > 0$  at the nadir, in retrospect, it is likely that tilting also contributed to  $\zeta$  growth (see their Fig. 11a), as described herein.

the edge of cold pools, Markowski et al. (2014) found upward tipping of the vorticity in descending flow (Davies-Jones and Brooks 1993) to account for the vertical vorticity of the sheet. Similar comments apply to the study of near-surface vertical vorticity in idealized downdrafts (Parker and Dahl 2015).

Davies-Jones and Markowski (2013) showed that tilting of horizontal vorticity by a gust front fails to yield significant near-surface vorticity. In that case, the horizontal vorticity is diminished as the flow decelerates *ahead* of the gust front. In the present case, in contrast, the flow is along and *behind* the gust front toward an updraft. In this case, the horizontal vorticity is increased as the flow accelerates toward the updraft, and tilting can produce significant near-ground vertical vorticity.

In summary, the present study considers the vorticity dynamics at vertical heights below the lowest grid levels in the typical idealized simulation of a supercell thunderstorm. The simulation of the idealized-supercell-like flow of MR14 is rerun with much higher vertical resolution near the surface. An analysis of the vorticity following the parcel that will acquire the largest vertical vorticity near the surface shows that, although there is upward tilting of horizontal vorticity just before the parcel reaches its nadir, it arrives there with essentially zero vertical vorticity. The subsequent growth of low-level vorticity following a parcel occurs in rising motion near the surface. The present analytical model shows that nonzero vertical vorticity at the nadir, while helpful, is not required for significant near-ground vertical vorticity in updraft.

*Acknowledgments.* Thanks go to Morris Weisman for his comments on the first draft of this manuscript. Official reviews by Bob Davies-Jones, Johannes Dahl, and an anonymous reviewer are gratefully acknowledged. PMM acknowledges Matt Parker, Erik Rasmussen, and Yvette Richardson for helpful discussions relating to this work. PMM is supported by NSF Grant AGS-1536460.

#### REFERENCES

- Adlerman, E. J., K. K. Droegemeier, and R. Davies-Jones, 1999: A numerical simulation of cyclic mesocyclogenesis. *Mon. Wea. Rev.*, **130**, 2045–2069, doi:10.1175/1520-0469(1999)056<2045:ANSOCM>2.0.CO;2.
- Bryan, G. H., and H. Morrison, 2012: Sensitivity of a simulated squall line to horizontal resolution and parameterization of microphysics. *Mon. Wea. Rev.*, **140**, 202–225, doi:10.1175/MWR-D-11-00046.1.
- Dahl, J. M. L., 2015: Near-ground rotation in simulated supercells: On the robustness of the baroclinic mechanism. *Mon. Wea. Rev.*, **143**, 4929–4942, doi:10.1175/MWR-D-15-0115.1.

- , M. D. Parker, and L. J. Wicker, 2012: Uncertainties in trajectory calculations within near-surface mesocyclones of simulated supercells. *Mon. Wea. Rev.*, **140**, 2959–2966, doi:[10.1175/MWR-D-12-00131.1](https://doi.org/10.1175/MWR-D-12-00131.1).
- , —, and —, 2014: Imported and storm-generated near-ground vertical vorticity in a simulated supercell. *J. Atmos. Sci.*, **71**, 3027–3051, doi:[10.1175/JAS-D-13-0123.1](https://doi.org/10.1175/JAS-D-13-0123.1).
- Davies-Jones, R., 2008: Can a descending rain curtain in a supercell instigate tornadogenesis barotropically? *J. Atmos. Sci.*, **65**, 2469–2497, doi:[10.1175/2007JAS2516.1](https://doi.org/10.1175/2007JAS2516.1).
- , 2015: A review of supercell and tornado dynamics. *Atmos. Res.*, **158–159**, 274–291, doi:[10.1016/j.atmosres.2014.04.007](https://doi.org/10.1016/j.atmosres.2014.04.007).
- , and H. E. Brooks, 1993: Mesocyclogenesis from a theoretical perspective. *The Tornado: Its Structure, Dynamics, Prediction, and Hazards*, C. Church et al., Eds., Amer. Geophys. Union, 105–114, doi:[10.1029/GM079p0105](https://doi.org/10.1029/GM079p0105).
- , and P. M. Markowski, 2013: Lifting of ambient air by density currents in sheared environments. *J. Atmos. Sci.*, **70**, 1204–1215, doi:[10.1175/JAS-D-12-0149.1](https://doi.org/10.1175/JAS-D-12-0149.1).
- Dutton, J. A., 1976: *The Ceaseless Wind: An Introduction to the Theory of Atmospheric Motion*. McGraw-Hill, 579 pp.
- Klemp, J. B., 1987: Dynamics of tornadic thunderstorms. *Annu. Rev. Fluid Mech.*, **19**, 369–402, doi:[10.1146/annurev.fl.19.010187.002101](https://doi.org/10.1146/annurev.fl.19.010187.002101).
- , and R. B. Wilhelmson, 1978: The simulation of three-dimensional convective storm dynamics. *J. Atmos. Sci.*, **35**, 1070–1096, doi:[10.1175/1520-0469\(1978\)035<1070:TSOTDC>2.0.CO;2](https://doi.org/10.1175/1520-0469(1978)035<1070:TSOTDC>2.0.CO;2).
- , and R. Rotunno, 1983: A study of the tornadic region within a supercell thunderstorm. *J. Atmos. Sci.*, **40**, 359–377, doi:[10.1175/1520-0469\(1983\)040<0359:ASOTTR>2.0.CO;2](https://doi.org/10.1175/1520-0469(1983)040<0359:ASOTTR>2.0.CO;2).
- Markowski, P. M., and Y. Richardson, 2010: *Mesoscale Meteorology in Midlatitudes*. Wiley-Blackwell, 430 pp.
- , and —, 2014: The influence of environmental low-level shear and cold pools on tornadogenesis: Insights from idealized simulations. *J. Atmos. Sci.*, **71**, 243–275, doi:[10.1175/JAS-D-13-0159.1](https://doi.org/10.1175/JAS-D-13-0159.1).
- , —, and G. Bryan, 2014: The origins of vortex sheets in a simulated supercell thunderstorm. *Mon. Wea. Rev.*, **142**, 3944–3954, doi:[10.1175/MWR-D-14-00162.1](https://doi.org/10.1175/MWR-D-14-00162.1).
- Parker, M. D., and J. M. L. Dahl, 2015: Production of near-surface vertical vorticity by idealized downdrafts. *Mon. Wea. Rev.*, **143**, 2795–2816, doi:[10.1175/MWR-D-14-00310.1](https://doi.org/10.1175/MWR-D-14-00310.1).
- Rotunno, R., 1981: On the evolution of thunderstorm rotation. *Mon. Wea. Rev.*, **109**, 577–586, doi:[10.1175/1520-0493\(1981\)109<0577:OTEOTR>2.0.CO;2](https://doi.org/10.1175/1520-0493(1981)109<0577:OTEOTR>2.0.CO;2).
- , and J. B. Klemp, 1985: On the rotation and propagation of simulated supercell thunderstorms. *J. Atmos. Sci.*, **42**, 271–292, doi:[10.1175/1520-0469\(1985\)042<0271:OTRAPO>2.0.CO;2](https://doi.org/10.1175/1520-0469(1985)042<0271:OTRAPO>2.0.CO;2).